

# High-sensitivity in situ QCLAS-based ammonia concentration sensor for high-temperature applications

W. Y. Peng<sup>1</sup>  · R. Sur<sup>1</sup> · C. L. Strand<sup>1</sup> · R. M. Spearrin<sup>1</sup> · J. B. Jeffries<sup>1</sup> · R. K. Hanson<sup>1</sup>

Received: 9 March 2016 / Accepted: 6 June 2016 / Published online: 25 June 2016  
© Springer-Verlag Berlin Heidelberg 2016

**Abstract** A novel quantum cascade laser (QCL) absorption sensor is presented for high-sensitivity in situ measurements of ammonia (NH<sub>3</sub>) in high-temperature environments, using scanned wavelength modulation spectroscopy (WMS) with first-harmonic-normalized second-harmonic detection (scanned WMS-2f/1f) to neutralize the effect of non-absorption losses in the harsh environment. The sensor utilized the sQ(9,9) transition of the fundamental symmetric stretch band of NH<sub>3</sub> at 10.39 μm and was sinusoidally modulated at 10 kHz and scanned across the peak of the absorption feature at 50 Hz, leading to a detection bandwidth of 100 Hz. A novel technique was used to select an optimal WMS modulation depth parameter that reduced the sensor's sensitivity to spectral interference from H<sub>2</sub>O and CO<sub>2</sub> without significantly sacrificing signal-to-noise ratio. The sensor performance was validated by measuring known concentrations of NH<sub>3</sub> in a flowing gas cell. The sensor was then demonstrated in a laboratory-scale methane-air burner seeded with NH<sub>3</sub>, achieving a demonstrated detection limit of 2.8 ± 0.26 ppm NH<sub>3</sub> by mole at a path length of 179 cm, equivalence ratio of 0.6, pressure of 1 atm, and temperatures of up to 600 K.

## 1 Introduction

Ammonia (NH<sub>3</sub>) is an important species in a number of high-temperature industrial processes, including the

Haber-Bosch process, the organic synthesis of numerous compounds, and the selective catalytic reduction (SCR) of nitric oxide (NO<sub>x</sub>) emissions in combustion-based energy systems (e.g., gas turbines and diesel engines) [1]. In SCR, ammonia is typically injected into the combustion exhaust and allowed to react with the NO<sub>x</sub> species to form water vapor and nitrogen. NO<sub>x</sub> and NH<sub>3</sub> concentrations are directly correlated in such applications. If NH<sub>3</sub> is injected at a sub-optimal temperature or flow rate, the optimal NO<sub>x</sub> abatement is not attained; if too much NH<sub>3</sub> is added, unreacted NH<sub>3</sub> will remain in the exhaust and escape into the environment, known as ammonia slip [2, 3]. This poses a significant risk to the public as both NO<sub>x</sub> and NH<sub>3</sub> are toxic to public health and to the environment. To prevent sub-optimal operation of SCR systems, it is desirable to implement closed-loop control systems that can quickly respond to changing conditions within the SCR. A key element in such closed-loop systems is a real-time sensor for ammonia concentration. Unfortunately, common sampling-based speciation techniques either require high sampling flow rates to enable temporally resolved NH<sub>3</sub> concentration measurements (as in gas chromatography) or are slow by nature (as in Fourier transform infrared spectroscopy). Additionally, NH<sub>3</sub> adsorption onto the sampling manifolds can result in significant discrepancies between the measured and actual concentrations. Therefore, a high-sensitivity in situ sensor for trace quantities of NH<sub>3</sub> is needed to provide real-time monitoring of these industrial processes. To achieve this capability, laser absorption spectroscopy (LAS) is often used because of its significant advantages for in situ monitoring of gas properties associated with high temporal resolution, measurement sensitivity, and robustness against various forms of noise [4].

Several studies have demonstrated in situ LAS-based NH<sub>3</sub> sensors in high-temperature environments. Webber

✉ W. Y. Peng  
wypeng@stanford.edu

<sup>1</sup> High Temperature Gasdynamics Laboratory, 452 Escondido Mall, Bldg. 520, Thermosciences Division, Stanford University, Stanford, CA 94305, USA

et al. [5] demonstrated a 1.53  $\mu\text{m}$  external-cavity diode laser-based direct absorption spectroscopy sensor with a 22 ppm  $\text{NH}_3$  detection limit in an equivalence ratio ( $\phi$ ) of 0.7 ethylene-air combustion exhaust at 495 K. As the relative  $\text{NH}_3$  concentration is decreased, however, spectral interference from neighboring  $\text{CO}_2$  and  $\text{H}_2\text{O}$  transitions becomes more prominent and renders this sensor unsuitable for use at higher temperatures and lower  $\text{NH}_3$  concentrations. Chao et al. [6] demonstrated a 15 ppm detection limit using a 2.25  $\mu\text{m}$  distributed feedback (DFB) diode laser in a  $\phi = 0.9\text{--}1.1$  ethylene-air burner exhaust at 620 K. There were only trace quantities of unburned hydrocarbons in this application, however. At higher hydrocarbon concentrations on the order of 100 ppm expected in practical environments, spectral interference from the strong hydrocarbon C–H symmetric stretch bands at 2.25  $\mu\text{m}$  is expected to significantly degrade sensor performance. More recently, Stritzke et al. [7] demonstrated detection limits of 50–70 ppm also using DFB diode lasers at 2.20  $\mu\text{m}$  in 800 K exhaust with high  $\text{H}_2\text{O}$  and  $\text{CO}_2$  concentrations (15 % each). For  $\text{NH}_3$  concentrations below this detection limit, however, this sensor fails because of strongly interfering  $\text{H}_2\text{O}$  and  $\text{CO}_2$  features.

The recent availability of quantum cascade lasers (QCLs) in the mid-infrared (MIR) region (4–16  $\mu\text{m}$ ) has enabled the development of compact spectroscopic sensors that access the strongest fundamental rovibrational absorption bands of  $\text{NH}_3$ . Due to the strength of these bands, highly sensitive  $\text{NH}_3$  measurements have been demonstrated by several authors in atmospheric sensing (e.g., [8–10] and references within) and in clinical analysis of human breath (e.g., [11–13]). None, however, have extended this technology to sensitive MIR  $\text{NH}_3$  measurements in high-temperature environments. In this research, we present a QCLAS-based  $\text{NH}_3$  sensor that achieved a detection limit of  $2.8 \pm 0.26$  ppm  $\text{NH}_3$  by mole at a measurement rate of 100 Hz in a  $\phi = 0.6$  methane ( $\text{CH}_4$ )-air high-temperature exhaust flow at temperatures of up to 600 K. These thermodynamic conditions reflect the typical environment encountered in the SCR section of natural-gas-powered gas turbines, while the measurement rate was set by the temporal resolution required to capture high-frequency transients within the SCR, especially during turbine start-up. This sensor used scanned wavelength modulation spectroscopy with first-harmonic-normalized second-harmonic detection (scanned WMS-2f/1f) to neutralize the effects of non-absorbing transmission losses, beam-steering, and 1/f noise sources in the exhaust stream. The demonstrated detection limit represents an order-of-magnitude improvement in sensitivity over previous NIR-based high temperature  $\text{NH}_3$  sensors.

The novelty of the current detection scheme lies in: (1) the selection of a previously unused  $\text{NH}_3$  transition near 10.39  $\mu\text{m}$  that is strong and relatively free of spectral

interference from  $\text{H}_2\text{O}$  and  $\text{CO}_2$  transitions at high temperature compared to transitions previously showcased in the literature [5–7, 14], and (2) the use of a novel procedure for selecting scanned-WMS tuning parameters that minimizes sensitivity to fluctuations in the concentration of spectral interferers without significantly sacrificing signal-to-noise ratio (SNR) of the WMS lineshapes. Experimentally derived spectroscopic parameters of the transitions used for this sensor were reported by Sur et al. [15], thus enabling higher-accuracy  $\text{NH}_3$  spectral models than current databases (e.g., HITRAN). Measurements of  $\text{NH}_3$  seeded in a laboratory-scale  $\text{CH}_4$ -air burner were made to validate the WMS model and to demonstrate sensor performance for high-temperature applications.

## 2 Theory

The  $\text{NH}_3$  sensor is based on the principles of laser absorption spectroscopy (LAS) employing the wavelength modulation spectroscopy (WMS) methodology for signal recovery and interpretation. These concepts are introduced briefly in the next two sections:

### 2.1 Absorption spectroscopy

The theory of laser absorption spectroscopy is well documented in the literature and only a brief description is reproduced here to define units and convention. More detailed discussions can be found in other works [16, 17]. The Beer–Lambert law governs the spectral transmissivity,  $\tau_\nu$ , of monochromatic radiation at frequency  $\nu$  ( $\text{cm}^{-1}$ ) through a gaseous absorbing medium:

$$\tau_\nu = \left( \frac{I}{I_0} \right)_\nu = \exp(-\alpha_\nu) \quad (1)$$

where  $I_0$  is the incident beam intensity,  $I$  is the transmitted beam intensity, and  $\alpha_\nu$  is the spectral absorbance given by

$$\alpha_\nu = \sum_{i,j} PL\chi_i S_{ij}(T)\phi_{ij,\nu}(T, P, \vec{\chi}) \quad (2)$$

for pressure,  $P$  (atm), temperature,  $T$  (K), and mole fraction vector,  $\vec{\chi}$ , along a uniform line of sight of length  $L$  (cm) between the incident and measurement locations.  $S_{ij}$  ( $\text{cm}^{-2} \cdot \text{atm}^{-1}$ ) and  $\phi_{ij,\nu}$  (cm) represent the linestrength and lineshape function, respectively, for the  $j$ th absorption transition of the  $i$ th species. The Voigt function was used to model the lineshapes of the transitions, which considers the combined effects of Doppler and collisional broadening on the spectra. These effects are characterized by the Doppler broadening full width at half maximum (FWHM),  $\Delta\nu_D$  ( $\text{cm}^{-1}$ ), and the collisional-broadening FWHM,  $\Delta\nu_C$  ( $\text{cm}^{-1}$ ), given by

$$\Delta\nu_d = 7.162 \times 10^{-7} \nu_0 \sqrt{\frac{T}{M}} \quad (3)$$

$$\Delta\nu_c = 2P \sum_i \chi_i \gamma_{i,0} \left(\frac{T_0}{T}\right)^{n_i} \quad (4)$$

where  $\nu_0$  is the center frequency ( $\text{cm}^{-1}$ ) of the transition,  $M$  is the molecular mass of the absorbing species ( $\text{g/mol}$ ),  $\gamma_{i,0}$  ( $\text{cm}^{-1} \text{atm}^{-1}$ ) is the collisional-broadening half width half maximum (HWHM) parameter for the  $i$ th collisional partner at a reference temperature  $T_0$ , and  $n_i$  is the temperature-dependence exponent of the broadening parameter. More information regarding the Voigt function can be found in [18]. With all spectroscopic parameters and thermodynamic conditions known, concentration can be inferred by measuring  $\tau_\nu$ .

## 2.2 Scanned WMS-2f/1f

Scanned wavelength modulation spectroscopy (scanned WMS) is a laser absorption sensing technique that is tolerant to noise and immune from several known difficulties associated with commonly used direct absorption spectroscopy techniques. A short description is provided here—we refer the reader to other works [17, 19–23] for more thorough discussions on WMS theory. In scanned WMS, the laser optical frequency is temporally tuned about some mean optical frequency corresponding to a transition line-center,  $\bar{\nu}$ , of the target species using a combination of a high-frequency sinusoidal modulation at frequency  $f_m$  and a lower frequency scan at frequency  $f_s$ . The instantaneous optical frequency is expressed as

$$\nu(t) = \bar{\nu} + a_m \cos(2\pi f_m t + \phi_m) + a_s \cos(2\pi f_s t + \phi_s) \quad (5)$$

where  $a_m$  ( $\text{cm}^{-1}$ ) and  $a_s$  ( $\text{cm}^{-1}$ ) are the modulation and scan depths, respectively, while  $\phi_m$  and  $\phi_s$  are temporal phases of the optical frequency tuning. The corresponding non-absorbing laser intensity tuning is expressed as a Fourier series:

$$I_0(t) = \bar{I}_0 \left[ 1 + \sum_{k=1}^{\infty} i_{sk} \cos(2\pi k f_s t + \psi_{sk}) + i_{mk} \cos(2\pi k f_m t + \psi_{mk}) \right] \quad (6)$$

Here,  $\bar{I}_0$  represents the mean intensity, the  $i$  represents the mean-normalized intensity response amplitudes, and the  $\psi$  represents the temporal phases of the intensity waveform. The subscripts  $s$  and  $m$  correspond to the scan and modulation signals, respectively. For semiconductor lasers controlled by high-compliance current sources, the summation in Eq. 6 is typically truncated to only the two leading terms

without significant impact to the reconstructed waveform or to the results of the WMS post-processing method.

The  $n$ th harmonics ( $nf$ ) of the transmitted intensity relate directly to the absorption spectra and can be utilized to make measurements of unknown gas properties. These harmonics are extracted from the measured intensity waveforms via digital lock-in filters. In the WMS-2f/1f technique, the 2nd harmonic signal ( $2f$ ) is used for measurement, while the 1st harmonic signal ( $1f$ ) is used to normalize the  $2f$  signal to correct for non-absorption fluctuations in transmitted laser intensity during the measurement. With temperature, pressure, and optical path length known, the species concentration can be inferred from the transmitted intensity by matching a simulated WMS waveform to the measured WMS waveform as described in [22]. For this study, a peak-matching WMS fitting technique was employed, where the simulated  $\text{NH}_3$  concentration was varied until the measured and simulated WMS-2f/1f signals at transition linecenter matched.

## 3 Sensor design

### 3.1 Line selection

The primary criteria for line selection include strong absorbance and minimal spectral interference from other common high-temperature species, namely  $\text{H}_2\text{O}$  and  $\text{CO}_2$ . Fig. 1a shows the HITRAN 2012 [24] simulated absorption features of  $\text{NH}_3$ , plotted as linestrengths at the target temperature of 600 K from 1 to 14  $\mu\text{m}$ . Several distinct bands can be seen in the spectrum, the strongest of which are labeled. Although several transitions in the fundamental asymmetric stretch band (labeled  $\nu_3$ ) are equally as strong as transitions in the fundamental symmetric stretch band (labeled  $\nu_2$ ), the  $\nu_3$  band is dominated by strong and densely populated water transitions and is also susceptible to interference from the strong hydrocarbon C-H stretch bands. We therefore restricted our attention to the strong band of  $\nu_2$  transitions between 8.5 and 12  $\mu\text{m}$  as outlined in red in Fig. 1a.

Figure 1b shows the simulated absorption profile of  $\text{NH}_3$  from 8.5 to 12  $\mu\text{m}$ , overlaid by simulated profiles for 12 %  $\text{H}_2\text{O}$  and 6 %  $\text{CO}_2$  corresponding to their expected concentrations for a  $\phi = 0.6$   $\text{CH}_4$ -air flame at  $T = 600$  K,  $P = 1$  atm,  $L = 100$  cm. Note that 500 ppm of  $\text{NH}_3$  was used to simulate the  $\text{NH}_3$  spectrum here for the purpose of visibility at this scale—in reality, the  $\text{NH}_3$  band is almost completely masked by  $\text{H}_2\text{O}$  and  $\text{CO}_2$  interference at the target detection limit of 3 ppm, except within the sQ(J, K) manifold of the  $\nu_2$  band. In the sQ(J, K) manifold between 10.3 and 10.5  $\mu\text{m}$ , there is a region of strong, closely spaced  $\text{NH}_3$  transitions interspersed with relatively weak, widely

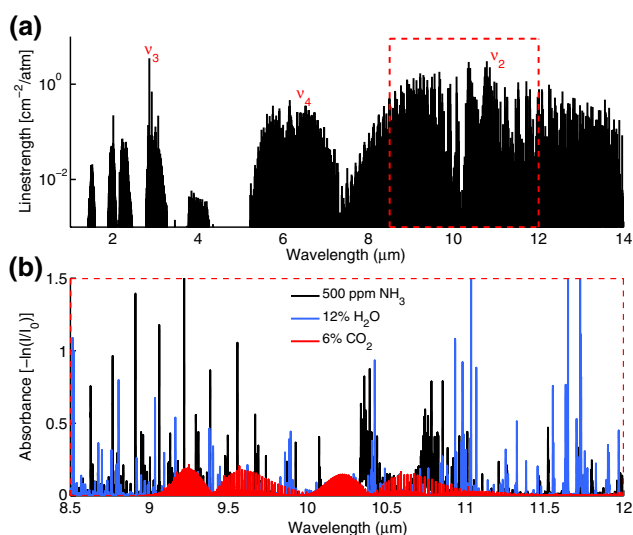


**Fig. 1** **a** Simulated  $\text{NH}_3$  linestrengths at 600 K from 1 to 14  $\mu\text{m}$  (HITRAN 2012 [24]). The surveyed spectral region of the fundamental symmetric stretch band ( $\nu_2$ ) is outlined in red-dashed lines. **b** Simulated absorption profile for 500 ppm  $\text{NH}_3$  in relation to simulated interference (HITEMP 2010 [25]) from expected  $\text{H}_2\text{O}$  and  $\text{CO}_2$  concentrations for a  $\phi = 0.6$   $\text{CH}_4$ -air flame at  $T = 600$  K,  $P = 1$  atm,  $L = 100$  cm for the surveyed spectral region

spaced  $\text{H}_2\text{O}$  and  $\text{CO}_2$  features. This region is also free of features from major hydrocarbons ( $\text{CH}_4$ ,  $\text{C}_2\text{H}_6$ ,  $\text{C}_3\text{H}_8$ , and  $\text{H}_2\text{CO}$ ), which makes this region suitable for use in practical systems where significant quantities of hydrocarbons in the process stream might be found. Due to the lack of spectral interference in this region, transitions in this region have been successfully utilized by several authors to measure part per billion levels of  $\text{NH}_3$  in atmospheric [8, 26, 27] and clinical breath sensing [13] applications. As a result, we focused the line selection process to this spectral region.

It should be noted that a transition near 8.91  $\mu\text{m}$  was initially identified to be quite suitable for measurements of  $\text{NH}_3$  in high-temperature environments according to the HITRAN 2012 database. However, after studying the local spectra of  $\text{H}_2\text{O}$  at high temperature using a Fourier transform infrared spectrometer (data is not presented here), a previously undocumented  $\text{H}_2\text{O}$  transition was discovered very close to the  $\text{NH}_3$  linecenter near 8.91  $\mu\text{m}$  and hence this transition was removed from further consideration for this sensor.

In WMS-2f/1f, the signal strength is most sensitive to the curvature of the absorption spectrum at the linecenter of the target transition [17]. Thus, transitions that are the most insensitive to spectral interference are transitions where the curvature at linecenter is the least perturbed by the presence of the interfering species. The strength of curvature perturbation,  $\Delta R$ , can be quantified by

$$\Delta R = \left| \frac{R_{up} - R_p}{R_{up}} \right| \quad (7)$$

where  $R_{up}$  and  $R_p$  are the curvatures of the absorption profile (approximated as  $d^2\alpha_\nu/d\nu^2$ , numerically evaluated using a second-order finite difference scheme) at  $\text{NH}_3$  linecenter for the unperturbed and perturbed cases, respectively. In general, the smaller  $\Delta R$  is, the less sensitive the WMS-2f/1f signal will be to spectral interference. We also applied a filter to remove transitions with peak absorbance below some minimum detectable absorbance. Based on prior experiments performed with similar lasers and detection systems, a minimum peak absorbance of  $3 \times 10^{-4}$  is generally required to achieve a SNR of 10 in the WMS-2f/1f signal. Thus, transitions that did not meet this minimum absorbance criterion for 3 ppm  $\text{NH}_3$  at a path length of 100 cm were removed from consideration in the selection algorithm.

Among the transitions with attractive  $\Delta R$  values and with acceptable peak absorbance, we chose to further investigate the sQ(9,9) transition near 962.17  $\text{cm}^{-1}$  (10.393  $\mu\text{m}$ ). Figure 2 shows the simulated absorption profile for  $\text{NH}_3$ ,  $\text{H}_2\text{O}$ , and  $\text{CO}_2$  at the target thermodynamic conditions described in the preceding section. The absorption spectrum in this region is composed of 4 overlapping  $\text{NH}_3$  transitions with sQ(9,9) making the dominant contribution. Surrounding the  $\text{NH}_3$  feature are relatively strong interference features from  $\text{H}_2\text{O}$  and  $\text{CO}_2$ ; however, because the  $\text{NH}_3$  feature resides within the tails of the absorption line-shapes of the interfering species, the interference does not significantly perturb the curvature at linecenter.

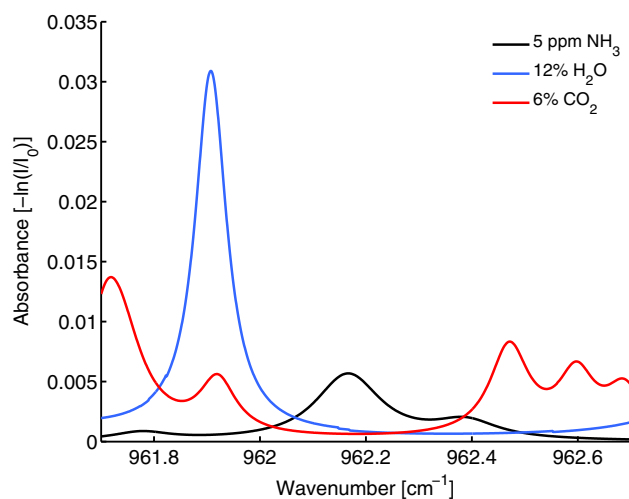


**Fig. 2** Simulated absorption spectra of  $\text{NH}_3$  (black),  $\text{H}_2\text{O}$  (blue), and  $\text{CO}_2$  (red) near 962.17  $\text{cm}^{-1}$  (10.393  $\mu\text{m}$ ) in a representative high-temperature environment ( $\text{CH}_4$ -air  $\phi = 0.6$ , 5 ppm  $\text{NH}_3$ ),  $T = 600$  K,  $P = 1$  atm,  $L = 100$  cm

**Table 1** Lower state energy ( $E$ ) and reference linestrengths of  $\text{NH}_3$  transitions near  $962.17 \text{ cm}^{-1}$ 

Transition	Linecenter ( $\text{cm}^{-1}$ )	$E''$ ( $\text{cm}^{-1}$ )	$S$ @ 296 K ( $\text{cm}^{-2}/\text{atm}$ )
sQ(10,7)	961.7762	907.9651	0.2195 <sup>(55)</sup>
sQ(10,6)	962.1443	955.1064	0.292 <sup>(15)</sup>
sQ(9,9)	962.1714	592.5867	3.672 <sup>(92)</sup>
sQ(9,8)	962.3884	655.6464	1.019 <sup>(26)</sup>

The superscripts denote the uncertainties in the measurements with respect to the last decimal digit (e.g., for sQ(10,7):  $S(296 \text{ K}) = 0.2195 \pm 0.055 \text{ cm}^{-2}/\text{atm}$ ). Reproduced from Sur et al. [15]

Unburnt ethylene ( $\text{C}_2\text{H}_4$ ) in the combustion exhaust could also be a source of interference for the selected  $\text{NH}_3$  transitions. If there were 5 ppm of  $\text{C}_2\text{H}_4$  and 5 ppm of  $\text{NH}_3$  present within the combustion exhaust and the interference due to  $\text{C}_2\text{H}_4$  was completely unaccounted for, HITRAN-based simulations suggest that the inferred  $\text{NH}_3$  concentration from the WMS- $2f/1f$  spectrum will be larger by 7 %, which is comparable to the estimated uncertainty of 8.5 % from other sources (see Sect. 4.4). However, Demayo et al. [28] found that the  $\text{C}_2\text{H}_4$  mole fraction was at most 708 ppb in the exhaust of stable industrial scale natural-gas-fired flames, and for three of the five cases they studied the  $\text{C}_2\text{H}_4$  mole fraction was less than 26 ppb. Since the target application of this sensor is for  $\text{NH}_3$  slip monitoring after SCR treatment of natural-gas-fired gas turbine exhaust,  $\text{C}_2\text{H}_4$  is not anticipated to be an important source of interference for the selected  $\text{NH}_3$  transitions. However, if this sensor was to be used for  $\text{NH}_3$  monitoring in the exhaust of heavier hydrocarbon fuels (e.g., Jet-A or liquified petroleum) where  $\text{C}_2\text{H}_4$  mole fractions can be on the order of 10 ppm (e.g., in a commercial jet engine as measured by Yelvington et al. [29]), the potential user is cautioned to evaluate the amount of  $\text{C}_2\text{H}_4$  in the exhaust and revisit the potential for interference in the  $\text{NH}_3$  measurements. We emphasize that as  $\text{NH}_3$  concentration is increased relative to  $\text{C}_2\text{H}_4$ , the

effects of  $\text{C}_2\text{H}_4$  interference on  $\text{NH}_3$  measurement uncertainty are reduced.

### 3.2 Spectroscopic parameters

The  $\text{NH}_3$  spectroscopic model used in this study included a composition-specific and temperature-dependent line broadening model. Spectroscopic parameters for the dominant transitions near sQ(9,9), including linestrength and broadening parameters for major collision partners in high-temperature environments ( $\text{N}_2$ ,  $\text{O}_2$ , Ar,  $\text{H}_2\text{O}$ , and  $\text{CO}_2$ ), were measured by Sur et al. [15] and are reproduced in Tables 1 and 2. A reference temperature of 296 K was used for all collisional-broadening parameters. For neighboring  $\text{H}_2\text{O}$  and  $\text{CO}_2$  transitions, spectroscopic parameters from the HITEMP 2010 [25] database were used.

### 3.3 Modulation depth optimization

In WMS techniques, the modulation depth parameter,  $a_m$ , (as defined in Eq. 5) plays a significant role in the SNR of the measured WMS signals. Conversely, the scan depth,  $a_s$ , does not have a significant impact on SNR as long as  $f_s$  is much smaller than  $f_m$ . In general,  $a_m$  is chosen such that the WMS- $2f$  signal at absorption linecenter is maximized. Rieker et al. [21] demonstrated that the optimal WMS- $2f$  signal at the linecenter of an isolated absorption feature can be achieved by selecting  $a_m$  equal to  $1.1\Delta\nu_{\text{tot}}$ , where  $\Delta\nu_{\text{tot}}$  is the total spectral broadening FWHM. As  $a_m$  is varied around this optimal value, the WMS- $2f$  signal is reduced because the sensor either under- or over-samples the absorption profile of the feature around linecenter, thus reducing the SNR of the WMS output.

Selecting an optimal  $a_m$  becomes a significantly more challenging proposition when the target absorption feature is in the presence of blended features [30] and neighboring interference features as shown in Fig. 2. For these situations, in addition to maximizing the WMS- $2f$  signal

**Table 2** Collision partner-specific broadening parameters for  $\text{NH}_3$  transitions near  $962.17 \text{ cm}^{-1}$ 

Transition	Quantity	$\text{N}_2$	$\text{O}_2$	$\text{CO}_2$	Ar	$\text{NH}_3$	$\text{H}_2\text{O}$
sQ(10,7)	$\gamma_{i,0}(\text{cm}^{-1}/\text{atm})$	0.087 <sup>(4)</sup>	0.044 <sup>(2)</sup>	0.202 <sup>(8)</sup>	0.033 <sup>(1)</sup>	0.443 <sup>(14)</sup>	0.263 <sup>(11)</sup>
	$n_i$	0.66 <sup>(5)</sup>	0.69 <sup>(5)</sup>	1.14 <sup>(5)</sup>	0.59 <sup>(5)</sup>	–	0.86 <sup>(10)</sup>
sQ(10,6)	$\gamma_{i,0}(\text{cm}^{-1}/\text{atm})$	0.104 <sup>(5)</sup>	0.034 <sup>(2)</sup>	0.216 <sup>(20)</sup>	0.033 <sup>(1)</sup>	0.423 <sup>(26)</sup>	0.257 <sup>(8)</sup>
	$n_i$	0.98 <sup>(10)</sup>	0.41 <sup>(10)</sup>	1.09 <sup>(10)</sup>	0.48 <sup>(10)</sup>	–	0.86 <sup>(20)</sup>
sQ(9,9)	$\gamma_{i,0}(\text{cm}^{-1}/\text{atm})$	0.109 <sup>(4)</sup>	0.051 <sup>(2)</sup>	0.214 <sup>(7)</sup>	0.042 <sup>(2)</sup>	0.57 <sup>(17)</sup>	0.307 <sup>(9)</sup>
	$n_i$	0.81 <sup>(5)</sup>	0.76 <sup>(5)</sup>	0.74 <sup>(5)</sup>	0.69 <sup>(5)</sup>	–	0.98 <sup>(10)</sup>
sQ(9,8)	$\gamma_{i,0}(\text{cm}^{-1}/\text{atm})$	0.098 <sup>(3)</sup>	0.048 <sup>(2)</sup>	0.187 <sup>(10)</sup>	0.039 <sup>(1)</sup>	0.511 <sup>(16)</sup>	0.316 <sup>(13)</sup>
	$n_i$	0.70 <sup>(5)</sup>	0.67 <sup>(5)</sup>	0.69 <sup>(5)</sup>	0.64 <sup>(5)</sup>	–	0.90 <sup>(10)</sup>

The superscripts denote the uncertainties in the measurements with respect to the last decimal digit (e.g., for sQ(10,7):  $\gamma_{\text{N}_2,0} = 0.087 \pm 0.004 \text{ cm}^{-1}/\text{atm}$ ). A reference temperature of 296 K was used. Reproduced from Sur et al. [15]

at linecenter, we also have to consider how sensitive the resulting WMS-2f/1f signal will be to the presence of interfering species. Here, we present a novel procedure for choosing an optimal WMS modulation depth in the presence of spectral interference.

Let  $F$  be a function of  $a_m$  that quantifies the inverse of the WMS signal strength, defined as

$$F(a_m) = \frac{S_{2f,\max}}{S_{2f}(a_m)} \tag{8}$$

where  $S_{2f}$  is the total interference-free WMS-2f signal for some known concentration of  $\text{NH}_3$  at the  $\text{NH}_3$  transition linecenter for some value of  $a_m$  accessible by the laser and  $S_{2f,\max}$  is the maximum possible interference-free WMS-2f signal. Using Eq. 8, it was observed that the function  $F(a_m)$  is minimized at  $a_m = 1.1\Delta\nu_{\text{tot}}$  for an isolated transition, consistent with the results of Rieker et al. [21] Now let  $\sigma$  be another function of  $a_m$  that quantifies the perturbation to the WMS-2f/1f signal due to the presence of spectral interference, defined as

$$\sigma(a_m) = \left| \frac{S_{2f/1f,\text{intf}}(a_m, \bar{\phi}) - S_{2f/1f}(a_m)}{S_{2f/1f}(a_m)} \right| \tag{9}$$

where  $S_{2f/1f,\text{intf}}$  is the WMS-2f/1f signal evaluated at the  $\text{NH}_3$  transition linecenter in the presence of known concentrations of the interfering species specified by the expected mean equivalence ratio,  $\bar{\phi}$ . Equation 9 is similar to the definition of  $\Delta R$  in Eq. 7 in the sense that  $\sigma$  approaches 0 as the impact of the interfering transitions on the curvature at linecenter is reduced. In this definition of  $\sigma$ , however, the effect of  $a_m$  on the total WMS-2f/1f signal is explicitly considered. As  $a_m$  is increased, more of the interfering absorption tails of the  $\text{H}_2\text{O}$  and  $\text{CO}_2$  transitions (see Fig. 2: local  $\text{NH}_3$  and interference spectra) are sampled by the laser during each modulation cycle. The more the interference features are sampled, the stronger the distortion in the WMS-2f/1f signal, causing  $\sigma$  to rise with  $a_m$  in general.

Ideally,  $a_m$  should be chosen such that both  $F$  and  $\sigma$  are simultaneously minimized. Such an  $a_m$  does not generally exist, however, so a compromise value for optimal  $a_m$  (denoted as  $a_{m,\text{opt}}$ ) needs to be chosen. The strategy we chose to employ for this compromise approach is to select  $a_{m,\text{opt}} = \arg \min(C)$ , where  $C = \sigma F$  is the product of the two functions, which we call the cost function. This definition of  $C$  was chosen because it is unbiased to either of the functions and that, in general, the minimum of  $C$  corresponds to an  $a_m$  in between the minima of  $\sigma$  and  $F$ .

The final step in implementing this procedure is to determine the values of  $S_{2f}$ ,  $S_{2f/1f}$ , and  $S_{2f/1f,\text{intf}}$  as a function of  $a_m$ . This requires knowledge of the tuning properties of the laser. Here, we have employed a DFB QCL (Alpes Laser S.A.) that targets the sQ(9,9) transition chosen in

the previous section. The modulation depth and intensity tuning parameters for this laser are shown in Figs. 3 and 4, respectively, for  $f_m = 10$  kHz. The modulation depth was characterized using standard procedures involving a solid germanium Fabry-Pérot etalon (free spectral range =  $0.0162 \text{ cm}^{-1}$ ). These tuning parameters, along with the simulated absorption profiles for 3 ppm  $\text{NH}_3$  in a bath gas of 12 %  $\text{H}_2\text{O}$  and 6 %  $\text{CO}_2$  (corresponding to the equilibrium composition of a  $\bar{\phi} = 0.6$   $\text{CH}_4$ -air flame) at 600 K, 1 atm were fed into the WMS model to simulate  $S_{2f}$ ,  $S_{2f/1f}$ , and  $S_{2f/1f,\text{intf}}$  as a function of  $a_m$ . With these quantities known,  $\sigma$ ,  $F$ , and  $C$  were calculated and plotted against  $a_m$  in Fig. 5. The optimal  $a_m$  was found to be  $0.069 \text{ cm}^{-1}$ , which successfully compromises between the minimum of  $\sigma$  and  $F$ . The function values of  $F$  and  $\sigma$  at this modulation

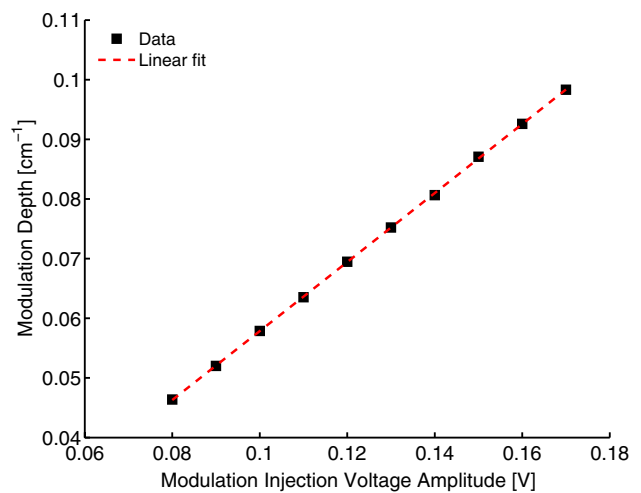


Fig. 3 Measured modulation depth as a function of modulation injection voltage amplitude

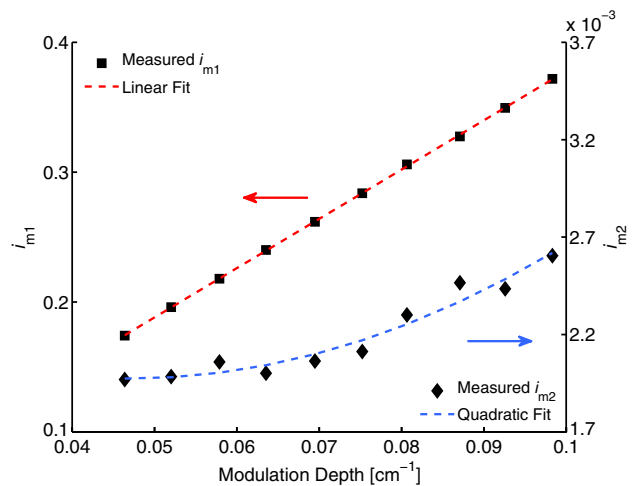
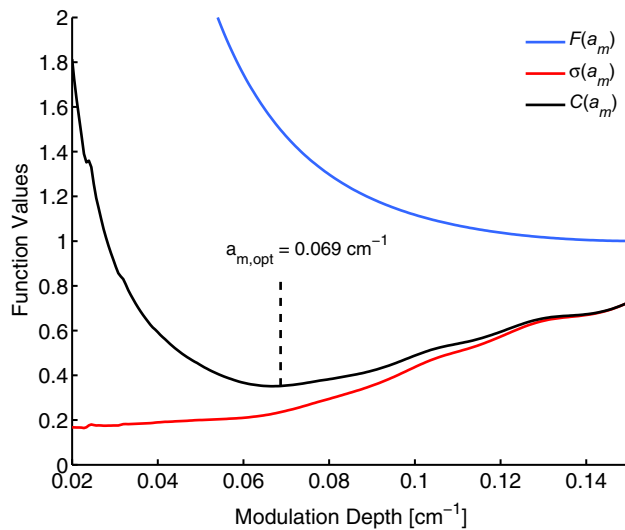


Fig. 4 Measured normalized modulation laser intensities ( $i_{m1}$  and  $i_{m2}$ ) as a function of modulation depth



**Fig. 5** Inverse WMS-2f signal strength ( $F$ , blue line),  $\text{NH}_3$  interference sensitivity ( $\sigma$ , red line), and cost function ( $C$ , black line) vs. modulation depth for a 3 ppm  $\text{NH}_3$  mixture in  $\text{CH}_4$ -air  $\phi = 0.6$  combustion exhaust at  $T = 600$  K,  $P = 1$  atm. The optimal modulation depth,  $a_{m,\text{opt}}$ , is shown in the black-dashed line

depth are 1.5 and 0.24, respectively. At the traditional optimal modulation depth of  $0.153 \text{ cm}^{-1}$  corresponding to  $F = 1$ ,  $\sigma$  was found to be 0.76, indicating that roughly 33 % of the maximum possible SNR is sacrificed to gain a threefold reduction in signal perturbation due to the presence of interference. This is a reasonable compromise for the purpose of maximizing sensor accuracy.

Figure 6a shows the simulated WMS-1f, 2f, and 2f/1f lineshapes near the target linecenter for 5 ppm  $\text{NH}_3$  at

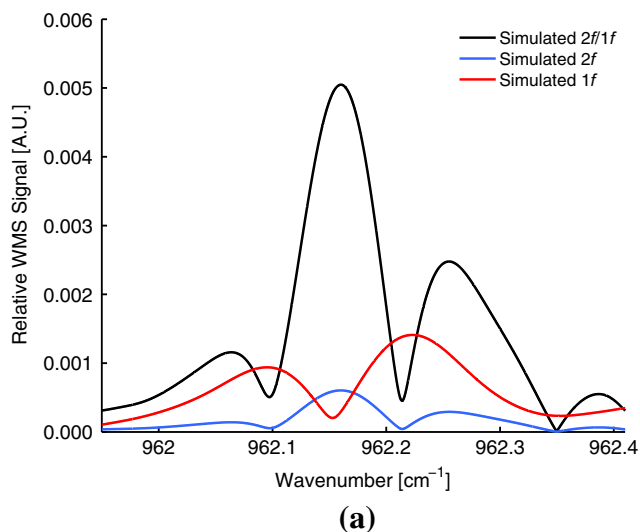


**Fig. 6 a** Simulated  $\text{NH}_3$  WMS spectra (2f, 1f, 2f/1f) near  $962.17 \text{ cm}^{-1}$ ,  $T = 600$  K,  $P = 1$  atm,  $\chi_{\text{NH}_3} = 5$  ppm. **b** Effect of  $\text{H}_2\text{O}$  and  $\text{CO}_2$  interference on the  $\text{NH}_3$  WMS-2f/1f spectra in a  $\phi = 0.6$

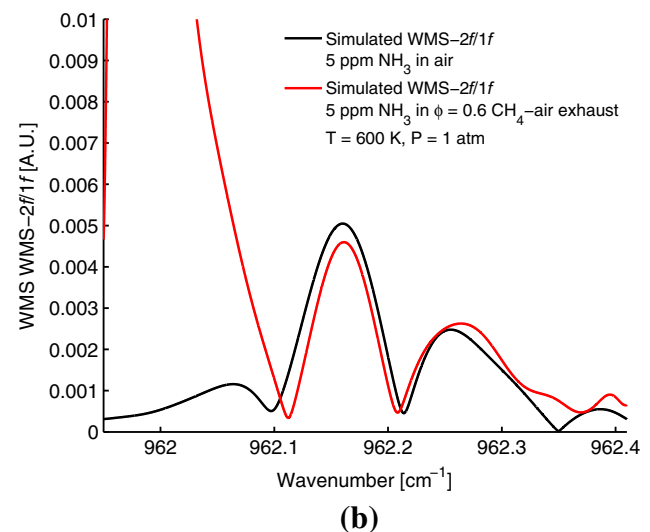
600 K and 1 atm using the optimal  $a_m$ . Figure 6b shows the simulated WMS-2f/1f lineshapes for 5 ppm  $\text{NH}_3$  with and without the presence of  $\text{H}_2\text{O}$  and  $\text{CO}_2$  (black and red curves, respectively). As shown, even in the presence of strong interference due to the  $\text{H}_2\text{O}$  and  $\text{CO}_2$  transitions near  $\text{NH}_3$  linecenter, the resulting WMS-2f/1f signal at linecenter is only perturbed by 10 %, demonstrating that this  $a_m$  optimization procedure successfully accounts for spectral interference from neighboring transition.

## 4 Sensor validation and demonstration

Two experiments were conducted to validate and demonstrate this sensor. First, the spectroscopic model used to convert the measured scanned WMS-2f/1f lineshapes into concentration values was validated by taking measurements of  $\text{NH}_3$  under known conditions in a flowing gas cell with air as the bath gas. Then, the sensor was demonstrated in a simulated high-temperature environment by taking  $\text{NH}_3$  measurements in an environmentally controlled laboratory-scale burner apparatus.

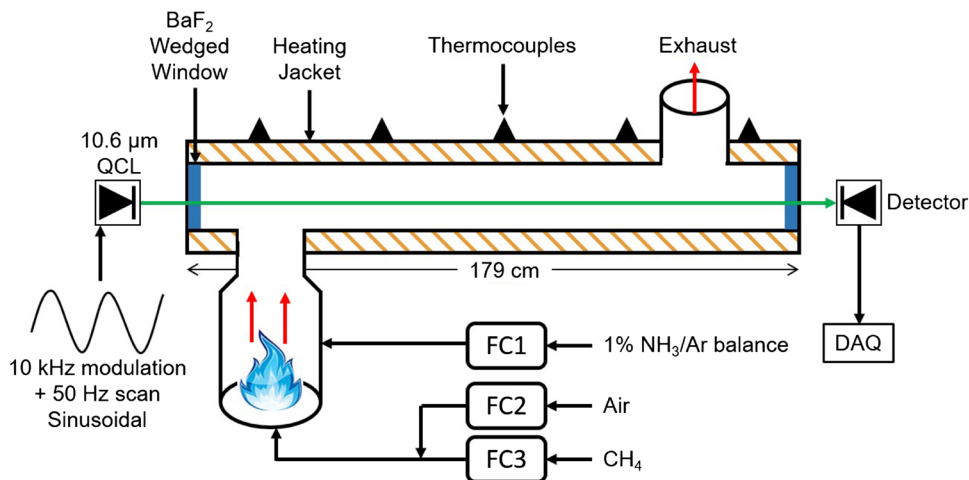
### 4.1 Experimental setup

Figure 7 shows a schematic of the burner apparatus used for both experiments.  $\text{NH}_3$  adsorbs onto most surfaces due to its polar nature, so to get accurately known  $\text{NH}_3$  concentration values for model validation, flowing  $\text{NH}_3$  mixtures were allowed to reach a steady concentration in the measurement cell (typically requiring 10–15 min). In the WMS validation experiments, room air was injected via a mass



$\text{CH}_4$ -air combustion exhaust at  $T = 600$  K,  $P = 1$  atm,  $L = 100$  cm seeded with 5 ppm  $\text{NH}_3$ . Both figures were generated using the optimized modulation depth of  $0.069 \text{ cm}^{-1}$

**Fig. 7** Schematic of the burner apparatus and optical configuration for performing  $\text{NH}_3$  WMS measurements in high-temperature exhaust



flow controller (Bronkhorst, labeled FC2) into an enclosed, temperature-controlled chamber at atmospheric pressure. Downstream of the air injector, a separate mass flow controller (FC1) injected a 1 %  $\text{NH}_3/\text{Ar}$  balance mixture and was allowed to mix thoroughly with the air before entering the detection section. The  $\text{NH}_3$  mixture originated from a new Praxair-certified gas bottle with proprietary coatings to reduce adsorption losses of  $\text{NH}_3$  to the inner wall. The detection section was a 179-cm-long cylindrical chamber with  $3^\circ$  wedged  $\text{BaF}_2$  windows on opposite ends and was wrapped with a feedback-controlled heating jacket. Five flow-embedded thermocouples were distributed uniformly along the detection section to enable temperature distribution measurements along the optical path. A similar flow procedure was used for the high-temperature exhaust experiment, except that  $\text{CH}_4$  (99.99 %, Praxair) was premixed with air and injected (FC3) into the lower combustion chamber and allowed to combust on a McKenna type sintered-metal disk flat-flame burner.

For all measurements presented in the following sections, the temperature distributions along the detection section were nearly constant along the middle 120 cm with gradual downward-facing parabolic tails toward the ends of the section. The difference between the temperature near the center and the ends did not exceed 50 K, which introduces some but generally negligible uncertainty to the measured  $\text{NH}_3$  mole fractions in comparison with other sources of uncertainty. The effects of the non-uniform temperature profiles on measurement uncertainty are discussed in Sect. 4.4.

The QCL output frequency was coarsely maintained by controlling the laser temperature using an Alpes Laser Model TC-3 temperature controller, while fine control of the output frequency and intensity was maintained by modulating the current with a high-compliance source (ILX Lightwave 3232). Electric current to the QCL was sinusoidally modulated using  $f_m = 10$  kHz and  $f_s = 50$  Hz,

providing a measurement rate of 100 Hz (2 measurements per scan period). The light was then transmitted through the detection section of the burner apparatus and detected on the opposite end via a photodetector (Vigo System S.A.) and stored on a PC. A lock-in amplifier coupled with a brick-wall low-pass filter at a cutoff frequency of  $20f_s$  was applied to the raw detected signals to obtain the harmonics of the WMS lineshape. Conversion to  $\text{NH}_3$  concentration values was accomplished via the peak-matching method described in Section 2.2.

#### 4.2 Scanned WMS- $2f/1f$ model validation in $\text{NH}_3$ -seeded air

To validate the WMS model, measurements of  $\text{NH}_3$  at a variety of concentrations in a bath gas of air were taken. Figure 8a shows one such set of measured (black line) and peak-matched (red-dashed line) WMS- $2f/1f$  lineshapes at a path-averaged temperature of 620 K and pressure of 1 atm. The two large peaks on either side of the optical tuning turn-around point at 15 ms (indicated by the green arrow) each corresponds to an  $\text{NH}_3$  measurement at linecenter. As can be seen, there is reasonable agreement between the measured and peak-matched WMS- $2f/1f$  lineshapes, demonstrating that the WMS simulation model was able to accurately reproduce the measured WMS lineshapes. Figure 8b compares the measured  $\text{NH}_3$  concentrations (black squares) against the  $\text{NH}_3$  concentrations obtained from relative flow rates in the burner cell. Each data point represents the mean  $\text{NH}_3$  concentration collected over on average of 5 min after the concentration reached steady state. The standard deviation ( $\sigma$ ) of the measurements over these 5 min periods was at most 1.2 % of the mean value. The concentrations measured using the optical sensor consistently agreed with the flow rate-based concentrations to within 1.5 %.



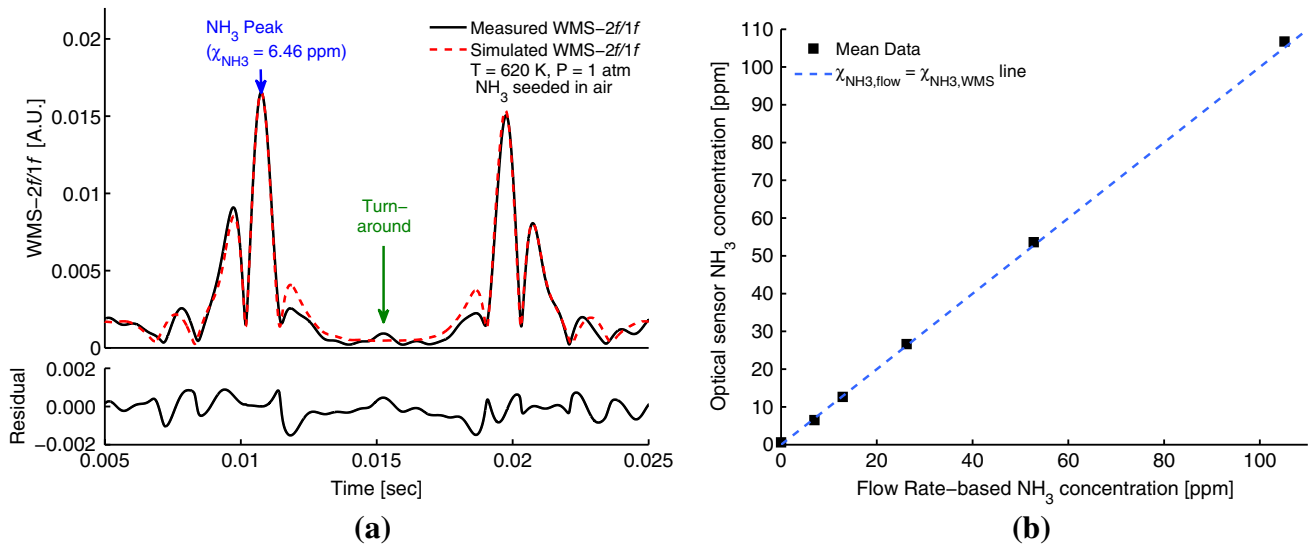


**Fig. 8** **a** Measured (black line) and peak-matched (red-dashed line) scanned WMS-2f/1f lineshapes for NH<sub>3</sub> seeded in air at  $T = 620$  K,  $P = 1$  atm,  $L = 179$  cm. Residuals of the fitting routine are shown

We now consider if the NH<sub>3</sub> concentrations calculated based on relative flow rates were actually representative of the NH<sub>3</sub> concentration along the detection section of the burner. In particular, it may be possible for significant quantities of NH<sub>3</sub> to dissociate or react with oxygen while in the heated section. CHEMKIN [31] reaction kinetics calculations were performed for 5–100 ppm NH<sub>3</sub> in a bath gas of air at the cell temperature of 620 K over the residence time of the NH<sub>3</sub> (~3.5 s for a nominal flow rate of 60 liters/min) within the heated section. The results indicated that the NH<sub>3</sub> concentration remains constant at these temperatures; therefore, we should expect the measured NH<sub>3</sub> concentration to be well represented by the flow rate-based calculations.

### 4.3 Sensor demonstration in a NH<sub>3</sub>-seeded high-temperature exhaust

To simulate the conditions expected in typical high-temperature environments, NH<sub>3</sub> was injected into the exhaust of a  $\phi = 0.6$  CH<sub>4</sub>-air flame, which is a representative global equivalence ratio found in gas turbine applications. Measurements of NH<sub>3</sub> concentration were then taken at a variety of NH<sub>3</sub> injection flow rates to evaluate the performance of the sensor. Figure 9a shows a set of measured (black line) and peak-matched (red-dashed line) WMS-2f/1f lineshapes at a path-averaged exhaust temperature of 592 K and pressure of 1 atm. Here, the WMS-2f/1f feature due to NH<sub>3</sub> is identified with the blue arrow, whereas the features due to H<sub>2</sub>O and CO<sub>2</sub> interference are identified by the red arrows. The green arrow marks the turn

below. **b** Measured NH<sub>3</sub> concentration versus flow rate-based NH<sub>3</sub> concentration (black squares) for the same conditions

around of the sinusoidal wavelength scan. We emphasize that it is not necessary to compensate for H<sub>2</sub>O and CO<sub>2</sub> interference when peak-matching the WMS-2f/1f spectra. The modulation depth optimization process ensures that the sensor accuracy will be reduced by at most 10 % (for 5 ppm NH<sub>3</sub> as demonstrated in Fig. 6b) if the measurements were processed without *a priori* knowledge of the H<sub>2</sub>O and CO<sub>2</sub> spectra. As the NH<sub>3</sub> concentration is increased, the perturbation to the WMS-2f/1f at NH<sub>3</sub> linecenter due to spectral interference becomes less pronounced, thereby increasing measurement accuracy as NH<sub>3</sub> concentration increases.

In practice, in order to maximize sensor accuracy, it is desirable to correct for H<sub>2</sub>O and CO<sub>2</sub> interference during post-processing. This can be achieved either by developing accurate experimental spectroscopic databases for the H<sub>2</sub>O and CO<sub>2</sub> transitions near the NH<sub>3</sub> linecenter or by measuring the H<sub>2</sub>O and CO<sub>2</sub> spectra prior to NH<sub>3</sub> injection (e.g., immediately upstream of the NH<sub>3</sub> injection point in an actual system). Currently available spectroscopic databases (e.g., HITEMP) could also be used for compensate for interference, but the accuracy of these databases is limited (generally >10 % uncertainty in linestrength, for example) in this range of wavelengths. In the measurements presented here, H<sub>2</sub>O and CO<sub>2</sub> interference was compensated for by measuring the H<sub>2</sub>O and CO<sub>2</sub> absorption profiles at the desired equivalence ratio prior to injecting the NH<sub>3</sub>. These absorption profiles were then fed into the NH<sub>3</sub> peak-matching WMS simulation model to produce the peak-matched WMS-2f/1f lineshape in Fig. 9a, which shows reasonable agreement with the measured lineshape.

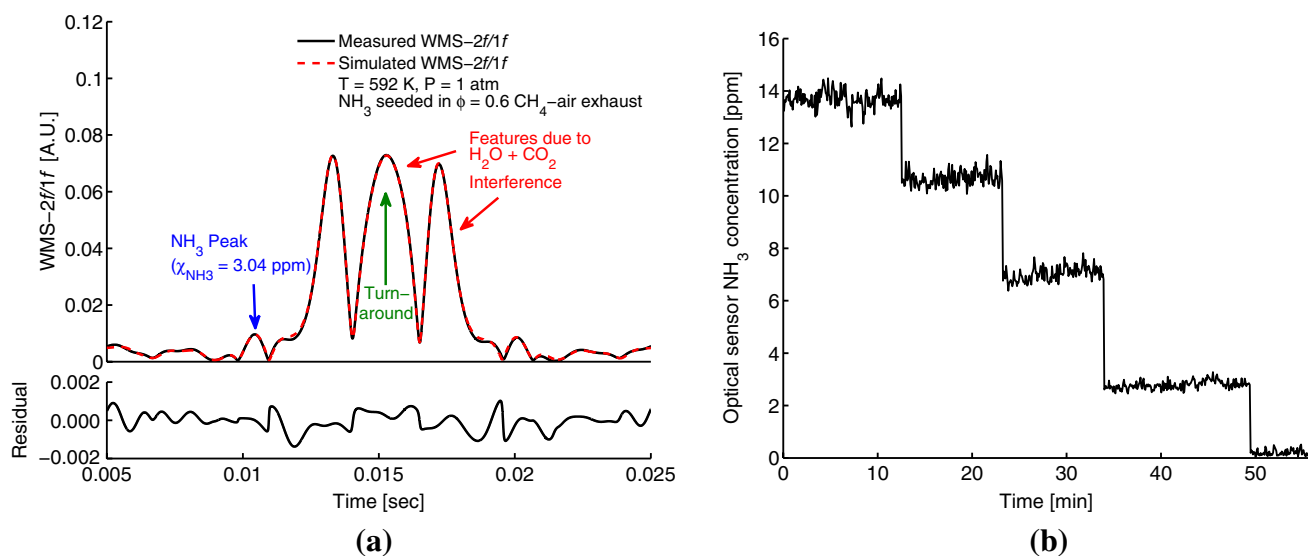


**Fig. 9** **a** Measured (*black line*) and peak-matched (*red-dashed line*) scanned WMS-2f/1f lineshapes for NH<sub>3</sub> seeded in a  $\phi = 0.6$  CH<sub>4</sub>-air combustion exhaust at  $T = 592$  K,  $P = 1$  atm,  $L = 179$  cm. Residuals

Figure 9b shows the measured NH<sub>3</sub> concentrations as a function of time in the burner, with distinct transitions in the measured concentration corresponding to step changes in the NH<sub>3</sub> injection flow rate. Because the NH<sub>3</sub> was injected fairly close to the burner's flame holder, an unknown amount of the injected NH<sub>3</sub> reacted with the residual oxygen and nascent NO<sub>x</sub> in the high temperature ( $\sim 1200$  K) exhaust. As a result, it was not possible to compare the measured NH<sub>3</sub> concentration against known values as previously shown in Fig. 8b. Each concentration step in the measurements presented in Fig. 9b had a  $2\sigma$  of no more than 6 % of the mean concentration at each injection flow rate, demonstrating the sensor's sensitivity and noise rejection capabilities down to a demonstrated detection limit of 2.8 ppm. Based on  $2\sigma$  of 0.2 ppm at the lowest-concentration set point, we project that this sensor is capable of reaching a detection limit of 0.5 ppm. However, because of the strong H<sub>2</sub>O and CO<sub>2</sub> interference, the WMS lineshape at the NH<sub>3</sub> linecenter becomes significantly distorted and loses any discernible peaks as the NH<sub>3</sub> concentration is lowered below around 1 ppm. Hence we conservatively conclude that the minimum detection limit of this sensor is around 1.5 ppm.

In most practical environments, the ambient gas composition will fluctuate during operation (e.g., due to unsteady fuel and air injection rates). Hence, it is important to understand how sensitive the measured NH<sub>3</sub> concentration is to fluctuations in the ambient H<sub>2</sub>O and CO<sub>2</sub> concentration. To assess this, the data presented in Fig. 9b was reprocessed using different H<sub>2</sub>O and CO<sub>2</sub> spectra corresponding to  $\phi = 0.6 \pm 0.06$ , representing a  $\pm 10$  % fluctuation intensity

of the fitting routine are shown below. **b** Continuously-measured NH<sub>3</sub> concentration versus time for the same burner conditions

in the global equivalence ratio in the exhaust plume. Practical combustion systems seldom experience fluctuations exceeding this magnitude; hence, this 10 % fluctuation intensity was conservatively chosen to assess sensor performance under worst-case scenarios. We observed that the reprocessed mean concentrations differed by no more than 3 % of the mean concentrations shown in Fig. 9b at each step along the ammonia injection concentration staircase. This provides further validation for the  $a_m$  optimization procedure presented in Sect. 3.3 because the small difference in reported NH<sub>3</sub> concentration demonstrates that this sensor is relatively insensitive to fluctuations in the concentrations of H<sub>2</sub>O and CO<sub>2</sub>.

#### 4.4 Uncertainty analysis

The uncertainty in the NH<sub>3</sub> mole fraction measurement,  $\sigma_\chi$ , can be quantified using the simple uncertainty propagation formula [32], assuming that the quantities used in the conversion process from WMS-2f/1f signal to the NH<sub>3</sub> mole fraction are uncorrelated.  $\sigma_\chi$  is defined as follows:

$$\sigma_\chi = \sqrt{\sum_i \left( \frac{\partial \chi}{\partial p_i} \right)^2 \sigma_{p_i}^2} \quad (10)$$

where  $p_i$  and  $\sigma_{p_i}$  denote the  $i$ th parameter involved in the signal conversion process and its uncertainty, respectively. In the peak-matching method as used in the preceding sections, these parameters include the linestrengths and broadening coefficients in the spectroscopic model for NH<sub>3</sub>, the temperature distribution, pressure, and optical

path length. Since the pressure and path length are well-known quantities, their uncertainties were not considered in Eq. 10.

Each partial derivative was evaluated numerically by introducing small perturbations (1 % of the nominal value was used here) to each parameter in the post-processing algorithm for the CH<sub>4</sub>-air measurement presented in Fig. 9 at a nominal NH<sub>3</sub> concentration of 3.04 ppm. The resulting changes in the converged values of  $\chi$  due to the perturbations were used to approximate the derivatives. The 3 % uncertainty due to an imposed 10 % fluctuation in the global equivalence ratio as discussed in Sect. 4.3 was included in the calculation for  $\sigma_\chi$ . Additionally, to quantify the uncertainty due to temperature non-uniformity, the data were reprocessed using a non-uniform temperature profile definition for the absorbance:

$$\alpha_v = \int_0^L \sum_{i,j} P \chi_i S_{ij}(T(x)) \phi_{ij,v}(T(x), P, \vec{\chi}) dx \quad (11)$$

Here, the temperature profile,  $T(x)$ , was approximated as the spline fit with parabolic end conditions of the five thermocouple readouts, whereas the composition vector,  $\vec{\chi}$ , and pressure were assumed to be constant throughout the detection section. The resulting difference between the calculated NH<sub>3</sub> mole fraction using Eq. 11 versus using Eq. 2 was used to estimate the uncertainty in  $\chi$  due to temperature non-uniformity.

The resulting  $\sigma_\chi$  was found to be 0.26 ppm, or 8.5 % of the calculated mole fraction for this measurement. Within this value for  $\sigma_\chi$ , the uncertainties in the temperature-dependence exponents were the largest contributors to the total uncertainty with a contribution of 0.12 ppm. This was followed by the uncertainties in the various  $\gamma_{i,0}$  and  $S_{i,0}$  with contributions of 0.09 and 0.02 ppm, respectively, while the imposed fluctuation in equivalence ratio contributed 0.03 ppm. Finally, the non-uniform temperature profile contributed only  $3 \times 10^{-4}$ , or 0.0012 %, to  $\sigma_\chi$ , which demonstrates that using a path-averaged definition for temperature when defining the absorbance is inconsequential to the calculated NH<sub>3</sub> mole fraction at least for the temperature profiles measured in this demonstration.

## 5 Conclusion

We report the development of an in situ, high sensitivity NH<sub>3</sub> concentration sensor for high-temperature applications based on a scanned WMS-2f/1f technique. The sensor utilized transitions in the the fundamental symmetric stretch band of NH<sub>3</sub> near 10.4  $\mu\text{m}$ , providing greater absorption and lower detection limits than other bands at shorter wavelengths in the infrared. A novel modulation

depth optimization technique was implemented to reduce the sensor's sensitivity to interfering absorption features from H<sub>2</sub>O and CO<sub>2</sub> in the high-temperature streams without a significant penalty in SNR of the WMS lineshapes. A DFB QCL centered at the sQ(9,9) transition near 10.39  $\mu\text{m}$  was modulated in intensity and optical frequency at 10 kHz and scanned across the absorption feature at 50 Hz to enable a measurement rate of 100 Hz. The WMS spectral model was validated by measuring known concentrations of NH<sub>3</sub> in a flowing, heated gas cell. The sensor was then demonstrated in a laboratory-scale CH<sub>4</sub>-air burner seeded with NH<sub>3</sub>, achieving a demonstrated detection limit of  $2.8 \pm 0.26$  ppm NH<sub>3</sub> at a path length of 179 cm, equivalence ratio of 0.6, pressure of 1 atm, and temperatures of up to 600 K. Broadly, this research serves to extend the applicability of high-sensitivity laser-based absorption sensing of NH<sub>3</sub> to a variety of high-temperature systems.

## References

1. M. Shelef, Chem. Rev. **95**(1), 209–225 (1995)
2. D.C. Mussatti, Technical report (2002)
3. K.A. Hossain, M.N. Mohd-Jaafar, K.B. Appalanidu, F.N. Ani, Environ. Technol. **26**(3), 251–260 (2005)
4. R.K. Hanson, Proc. Combust. Inst. **33**(1), 1–40 (2011)
5. M.E. Webber, D.S. Baer, R.K. Hanson, Appl. Opt. **40**(12), 2031–2042 (2001)
6. X. Chao, J.B. Jeffries, R.K. Hanson, Proc. Combust. Inst. **34**(2), 3583–3592 (2013)
7. F. Stritzke, O. Diemel, S. Wagner, Appl. Phys. B Lasers Opt. **119**(1), 143–152 (2015)
8. R. Lewicki, A. Kosterev, D.M. Thomazy, L. Gong, R. Griffin, F. Tittel, in *Laser Applications to Chemical, Security and Environmental Analysis* (Optical Society of America, 2010)
9. D.J. Miller, K. Sun, L. Tao, M.A. Khan, M.A. Zondlo, Atmos. Meas. Tech. **7**(1), 81–93 (2014)
10. J.D. Whitehead, I.D. Longley, M.W. Gallagher, Water Air Soil Pollut. **183**(1–4), 317–329 (2007)
11. K. Owen, A. Farooq, Appl. Phys. B **116**(2), 371–383 (2013)
12. Y.A. Bakhrkin, A.A. Kosterev, G. Wysocki, F.K. Tittel, T.H. Risby, J.D. Bruno, in *Laser Applications to Chemical, Security and Environmental Analysis* (Optical Society of America, 2008)
13. J. Manne, O. Sukhorukov, W. Jäger, J. Tulip, Appl. Opt. **45**(36), 9230–9237 (2006)
14. J.A. Silver, D.S. Bomse, A.C. Stanton, Appl. Opt. **30**(12), 1505–1511 (1991)
15. R. Sur, R.M. Spearrin, W.Y. Peng, C.L. Strand, J.B. Jeffries, G.M. Enns, R.K. Hanson, J. Quant. Spectrosc. Radiat. Transf. **175**, 90–99 (2016)
16. U. Platt, J. Stutz, in *Differential Optical Absorption Spectroscopy* (Springer, Berlin, Heidelberg, 2008)
17. P. Kluczynski, O. Axner, Appl. Opt. **38**(27), 5803–5815 (1999)
18. R.K. Hanson, R.M. Spearrin, C.S. Goldenstein, in *Spectroscopy and Optical Diagnostics for Gases*, 1st edn. (Springer, New York, 2015)
19. D.S. Bomse, A.C. Stanton, J.A. Silver, Appl. Opt. **31**(6), 718–731 (1992)
20. J. Reid, D. Labrie, Appl. Phys. B **26**(3), 203–210 (1981)
21. G.B. Rieker, J.B. Jeffries, R.K. Hanson, Appl. Opt. **48**(29), 5546–5560 (2009)

22. C.S. Goldenstein, C.L. Strand, I.A. Schultz, K. Sun, J.B. Jeffries, R.K. Hanson, *Appl. Opt.* **53**(3), 356–367 (2014)
23. K. Sun, X. Chao, R. Sur, C.S. Goldenstein, J.B. Jeffries, R.K. Hanson, *Meas. Sci. Technol.* **24**(12), 125203 (2013)
24. L.S. Rothman, I.E. Gordon, Y. Babikov, A. Barbe, D. Chris Benner, P.F. Bernath, M. Birk, L. Bizzocchi, V. Boudon, L.R. Brown, A. Campargue, K. Chance, E.A. Cohen, L.H. Coudert, V.M. Devi, B.J. Drouin, A. Fayt, J.M. Flaud, R.R. Gamache, J.J. Harrison, J.M. Hartmann, C. Hill, J.T. Hodges, D. Jacquemart, A. Jolly, J. Lamouroux, R.J. Le Roy, G. Li, D.a Long, O.M. Lyulin, C.J. Mackie, S.T. Massie, S. Mikhailenko, H.S.P. Müller, O.V. Naumenko, aV Nikitin, J. Orphal, V. Perevalov, A. Perrin, E.R. Polovtseva, C. Richard, M.A.H. Smith, E. Starikova, K. Sung, S. Tashkun, J. Tennyson, G.C. Toon, V.G. Tyuterev, G. Wagner, J. Quant. Spectrosc. Radiat. Transf. **130**, 4–50 (2013)
25. L. Rothman, I. Gordon, R. Barber, H. Dothe, R. Gamache, A. Goldman, V. Perevalov, S. Tashkun, J. Tennyson, J. Quant. Spectrosc. Radiat. Transf. **111**(15), 2139–2150 (2010)
26. M.B. Filho, M.G. da Silva, M.S. Sthel, D.U. Schramm, H. Vargas, A. Miklós, P. Hess, *Appl. Opt.* **45**(20), 4966–4971 (2006)
27. J. Manne, W. Jäger, J. Tulip, *Appl. Phys. B Lasers Opt.* **94**(2), 337–344 (2009)
28. T. Demayo, M. Miyasato, G. Samuelsen, *Symp. Int. Combust.* **27**(1), 1283–1291 (1998)
29. P.E. Yelvington, S.C. Herndon, J.C. Wormhoudt, J.T. Jayne, R.C. Miake-Lye, W.B. Knighton, C. Wey, *J. Propuls. Power* **23**(5), 912–918 (2007)
30. R. Sur, K. Sun, J.B. Jeffries, R.K. Hanson, *Appl. Phys. B Lasers Opt.* **115**(1), 9–24 (2014)
31. R. Kee, F. Rupley, J. Miller, Technical report, sep (1989)
32. H. Ku, *J. Res. Natl. Bur. Stand. Sect. C Eng. Instrum.* **70C**(4), 263–273 (1966)